

Article

The Scattering Coefficient for Shore-to-Air Bistatic High Frequency (HF) Radar Configurations as Applied to Ocean Observations

Zezone Chen ^{1,2,*}, Jian Li ¹ , Chen Zhao ¹ , Fan Ding ¹ and Xi Chen ¹

¹ School of Electronic Information, Wuhan University, Wuhan 430072, China; ivanlijian@whu.edu.cn (J.L.); zhaoc@whu.edu.cn (C.Z.); dingf242@whu.edu.cn (F.D.); ivanchenxi@whu.edu.cn (X.C.)

² School of Electronic Information and the Collaborative Innovation Center for Geospatial Technology, Wuhan University, Wuhan 430072, China

* Correspondence: chenzz@whu.edu.cn; Tel.: +86-133-0711-8527

Received: 28 October 2019; Accepted: 9 December 2019; Published: 11 December 2019



Abstract: To extend the scope of high frequency (HF) radio oceanography, a new HF radar model, named shore-to-air bistatic HF radar, has been proposed for ocean observations. To explore this model, the first-order scattering coefficient and the second-order electromagnetic scattering coefficient for shore-to-air bistatic HF radar are derived using the perturbation method. In conjunction with the contribution of the hydrodynamic component, the second-order scattering coefficient is derived. Based on the derived scattering coefficients, we analyzed the simulated echo Doppler spectra for various scattering angles and azimuthal angles, operation frequencies, wind speeds, and directions of wind, which may provide the guideline on the extraction of sea state information for shore-to-air bistatic HF radar. The singularities in the simulated echo Doppler spectra are discussed using the normalized constant Doppler frequency contours. In addition, the scattering coefficients of shore-to-air bistatic HF radar are compared with that of monostatic HF radar and land-based bistatic HF radar. The results verify the correctness of the proposed scattering coefficients. The model of shore-to-air bistatic HF radar is effective for ocean observations.

Keywords: shore-to-air bistatic HF radar; scattering coefficient; Doppler spectra

1. Introduction

High frequency (HF) radars have been efficient tools for ocean current, wave, and wind measurement, as well as target detection in the past four decades [1–4]. The interpretation of HF radio scattering from the ocean surface in monostatic and bistatic mode has been developed for several decades. A monostatic HF radar system consisting of a colocated transmitter and receiver operates in backscattering case. The first-order and second-order scattering coefficients for monostatic HF radar, derived by Barrick [5,6] based on Rice's work [7], have been widely accepted [8,9]. Subsequently, new monostatic HF electromagnetic scattering coefficients were proposed by Walsh using generalized functions from rough surfaces [10]. Hisaki and Tokuda also presented the monostatic results using the perturbation method when the illuminated area is finite [11,12]. In contrast to monostatic mode, bistatic HF radar system operates in the non-backscattering case in general. Johnstone presented the scattering coefficients of bistatic HF radar [13]. Anderson et al. [14] obtained a general solution to the bistatic scattering problem and have published a number of papers applying the formulae to various configurations and presenting computed spectra (e.g., [15]); however, they did not publish the details of their derivation. Other theoretical results were proposed by Anderson et al. and validated by field experiments [16–18]. Gill and Walsh developed the first-order and second-order scattering coefficients

for land-based bistatic HF radar based on a generalized function [19–21]. Some theoretical results were validated by Huang et al. using the wind direction measurements from the land-based bistatic HF radar [22]. Recently, Bernhardt gave an incoherent scattering coefficient related to the wave-height spectra for HF Ground-Ionosphere-Ocean-Space (GIOS) system [23].

Air-borne radars have the ability to detect large areas of the sea, which is meaningful to extend coverage for ocean radars [23–25]. To extend the scope of HF radio oceanography and meet the demands for large-area ocean observation, a new bistatic radar model so-called shore-to-air bistatic HF radar is designed for ocean observation [26]. The configuration is shown in Figure 1: The transmitter installed on the coast emits vertically polarized and narrow-beam electromagnetic waves to illuminate the ocean patch in a grazing incidence; the electromagnetic waves are scattered to a radar receiver deployed at an air platform (airplane or airship) owing to the rough sea surface; then the power spectra are estimated from radar echoes to extract the sea state information.

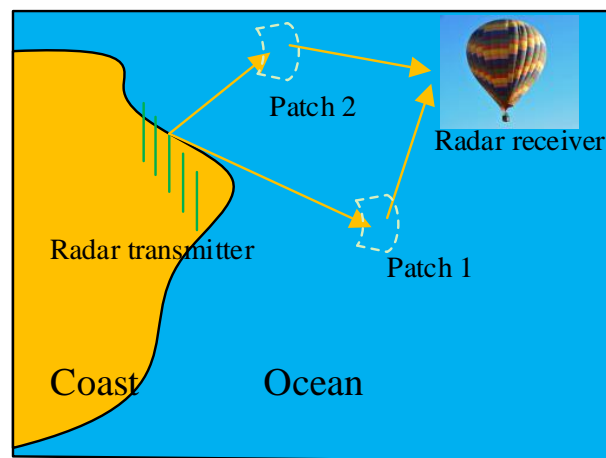


Figure 1. Model of shore-to-air bistatic high frequency (HF) radar.

In this paper, beginning with the establishment of the geometry of shore-to-air bistatic HF radar, the electric field intensity is obtained for the perfectly conducting rough ocean surface. Then the first-order and second-order electric field intensities are derived using Rice's method. The electric field near the observation point is obtained based on Kirchhoff theory [27]. The first-order and second-order electromagnetic scattering coefficients are given. Finally, the second-order scattering coefficient is obtained in conjunction with the contribution of hydrodynamic coupling. In order to validate the proposed scattering coefficients, the Doppler spectra are simulated in various scattering and azimuthal angles, operating frequencies, wind speeds, and wind directions.

This paper is organized as follows. The derivation of the first-order scattering coefficient and second-order scattering coefficient is given in Section 2. In Section 3, the simulated Doppler spectra in various operating modes and sea states are presented and analyzed. In Section 4, the singularities that occur in the simulated Doppler spectra are discussed. Conclusions are drawn in Section 5.

2. Model and Scattering Coefficients

2.1. The Geometry of Shore-To-Air Bistatic Hf Radar

The geometry of shore-to-air bistatic HF radar is shown in Figure 2. The x axis is assumed as the direction of the radar beam and the y axis is perpendicular to the x axis. The z axis is vertical to the sea surface. The incident electromagnetic wave (the wavenumber vector is \vec{k}_0) lies on x-z plane and the incident angle θ_i is the angle of the incident radar wave from the z axis. For the near-grazing incident wave, $\theta_i \approx \frac{\pi}{2}$. θ_s is the angle of the scattered radar wave (the wavenumber vector is \vec{k}_{sc}) from the z axis. φ_s is the azimuthal angle of the scattered radar wave from the incidence plane. The half angle

between the transmitter and the projection in the x-y plane of the receiver as viewed from the scatter patch is φ_0 , which satisfies the equation $\varphi_s = 180^\circ - 2\varphi_0$. The scattering coefficients of bistatic HF radar can be approximated as the sum of the first-order and second-order scattering coefficients

$$\sigma(\omega) = \sigma^{(1)}(\omega) + \sigma^{(2)}(\omega). \tag{1}$$

The equation of the perfectly conducting rough time-varying surface z can be expressed as a Fourier series:

$$z = f(x, y, t) = \sum_{mnl} P(m, n, l) \exp \left\{ \left(-j \left(\frac{2\pi m}{L} x + \frac{2\pi n}{L} y \right) - j\omega l t \right) \right\} \tag{2}$$

where the triple summation extends from $-\infty$ to $+\infty$ for l, m , and n , $P(m, n, l)$ are the Fourier expansion coefficients, and $T = 2\pi/\omega$ is the time period of the Fourier expansion and corresponds to the spatial period L (assumed to be large).

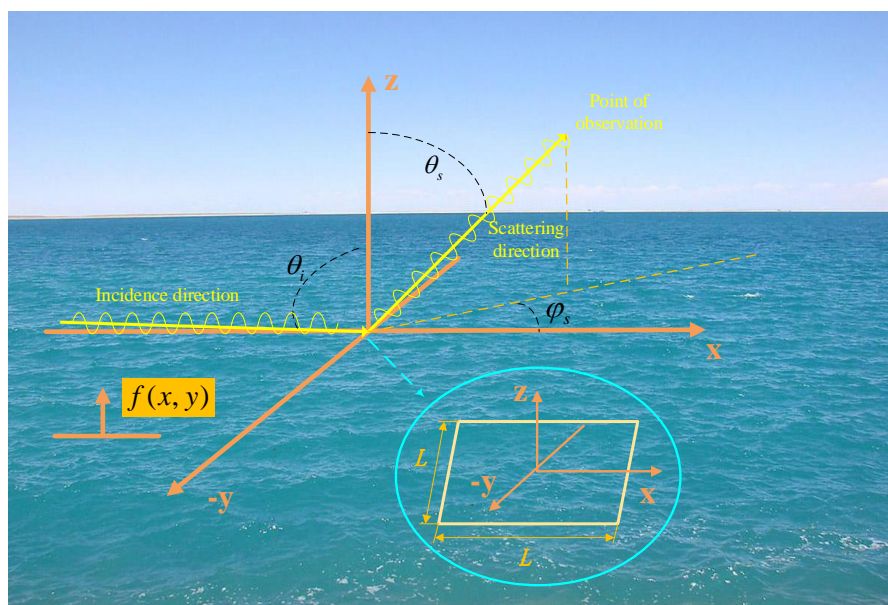


Figure 2. Geometry of shore-to-air bistatic HF radar.

2.2. Electromagnetic Scattering on the Rough Sea Surface

As shown in Figure 3, the magnitude of the vertical polarized incident wave is assumed to be unity. The electric-field vector of the incident wave can be expressed as:

$$\vec{E}_i(x, z, t) = (\cos\theta_i \hat{x} + \sin\theta_i \hat{z}) \exp(-jk_0 \sin\theta_i x + jk_0 \cos\theta_i z - j\omega_0 t) \tag{3}$$

where \hat{x} and \hat{z} are unit vectors along with the x axis and z axis, respectively, k_0 is the magnitude of radar radio wavenumber vector \vec{k}_0 , which is defined by the equation $k_0 = 2\pi/\lambda$ (λ is the wavelength of incident wave), ω_0 is the circular frequency, and t is the time.

The total scattering field is the sum of reflected fields for lack of surface roughness (specular scattering), and scattered fields due to the roughness of sea surface (nonspecular scattering). The specular scattering fields can be expressed as:

$$\vec{E}_1(x, z, t) = (-\cos\theta_i \hat{x} + \sin\theta_i \hat{z}) \exp(-jk_0 \sin\theta_i x - jk_0 \cos\theta_i z - j\omega_0 t). \tag{4}$$

The components of nonspecular scattering fields \vec{E}_2 in the x, y, and z directions can be expressed as:

$$\begin{cases} E_{2x} = \sum_{mnl} A_{mnl} E(m, n, z, l) \\ E_{2y} = \sum_{mnl} B_{mnl} E(m, n, z, l) \\ E_{2z} = \sum_{mnl} C_{mnl} E(m, n, z, l) \end{cases} \quad (5)$$

where $A_{mnl}, B_{mnl}, C_{mnl}$ are constants, and

$$E(m, n, z, l) = \exp(-j\frac{2\pi m}{L}x - j\frac{2\pi n}{L}y - jb(m, n)z - j\omega t). \quad (6)$$

The reflected wave field should satisfy the wave equation

$$b^2(m, n) = k_0^2 - (\frac{2\pi m}{L})^2 - (\frac{2\pi n}{L})^2 \quad (7)$$

and the divergence of the reflected field should be zero. Therefore, the coefficients $A_{mnl}, B_{mnl},$ and C_{mnl} are determined by the relation

$$\frac{2\pi m}{L}A_{mnl} + \frac{2\pi n}{L}B_{mnl} + b(m, n)C_{mnl} = 0. \quad (8)$$

$E(m, n, f, l)$ can be expanded as exponential series and A_{mnl} can be expressed using the perturbation method

$$E(m, n, f, l) = E(m, n, 0, l)[1 - jb(m, n)f + \dots] \quad (9)$$

$$A_{mnl} = A_{mnl}^{(1)} + A_{mnl}^{(2)} + \dots \quad (10)$$

where $f = z, A_{mnl}^{(1)}$ denotes $o(f),$ and $A_{mnl}^{(2)}$ denotes $o(f^2).$ $B_{mnl},$ and C_{mnl} can be expressed in a similar way.

The total electromagnetic field above the surface is expressed as a sum of the incident field and scattered field (including the specular scattered field and nonspecular scattered field). For the vertical polarized incident wave illuminating the ocean surface, the components of total electromagnetic fields $E(x, y, z, l)$ in the x, y, and z directions can be expressed as

$$E_x = 2j \cos \theta_i [\sin(k_0 \cos \theta_i z)] e^{-jk_0 \sin \theta_i x - j\omega_0 t} + \sum_{mnl} (A_{mnl}^{(1)} + A_{mnl}^{(2)} + \dots) [1 - jb(m, n)f + \dots] E(m, n, 0, l) \quad (11)$$

$$E_y = \sum_{mnl} (B_{mnl}^{(1)} + B_{mnl}^{(2)} + \dots) [1 - jb(m, n)f + \dots] E(m, n, 0, l) \quad (12)$$

$$E_z = 2 \sin \theta_i [\cos(k_0 \cos \theta_i z)] e^{-jk_0 \sin \theta_i x - j\omega_0 t} + \sum_{mnl} (C_{mnl}^{(1)} + C_{mnl}^{(2)} + \dots) [1 - jb(m, n)f + \dots] E(m, n, 0, l). \quad (13)$$

Substituting Formulas (11)–(13) into Rice boundary conditions [7] and separating the first-order and the second-order terms in these formulas, $A_{mnl}^{(1)}, B_{mnl}^{(1)}, C_{mnl}^{(1)}$ and $A_{mnl}^{(2)}, B_{mnl}^{(2)}, C_{mnl}^{(2)}$ can be solved. Then the electric components of the reflected electromagnetic waves can be obtained. According to the relationship between the electric field and the magnetic field of Maxwell's equation $\nabla \times \vec{E} = -j\omega\mu \vec{H},$ where ∇ denotes the Hamilton operator, and μ is the permeability to the volume material, the magnetic components of the reflected electromagnetic field can be obtained.

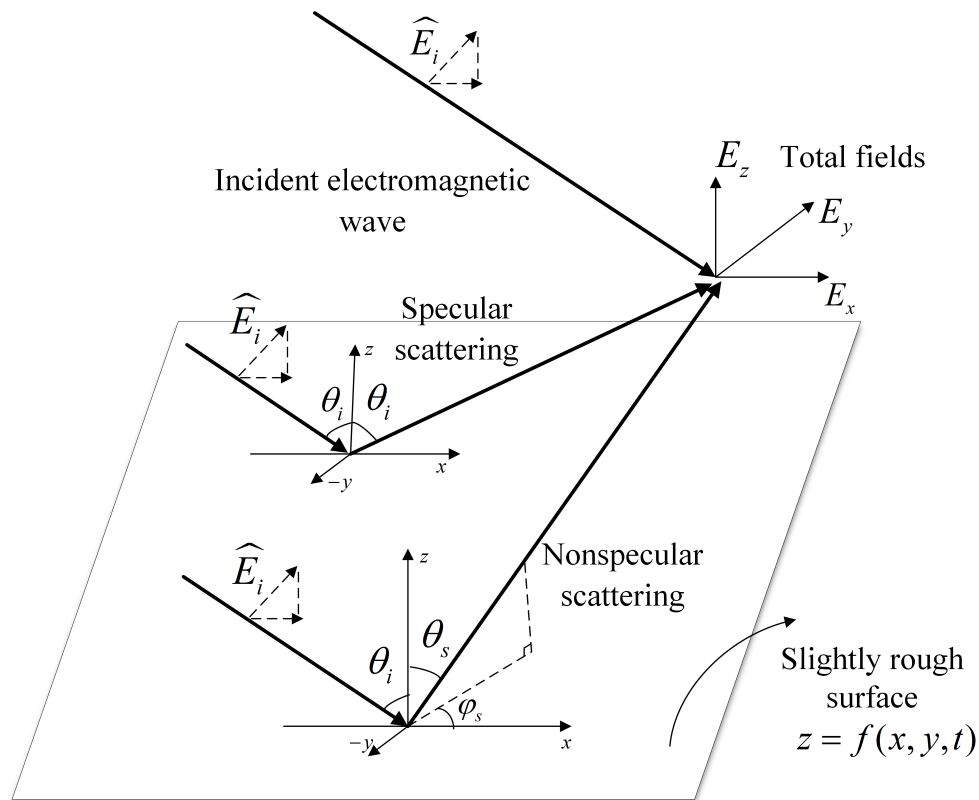


Figure 3. Fields above the sea surface. The total field is the sum of incident field, specular scattering field, and nonspecular scattering field. \hat{E}_i denotes the magnitude of vertical polarized incident wave, which is assumed to be unity.

The electric field of the observation point can be derived based on Kirchhoff theory [27]

$$\vec{E}(\vec{r}) = \nabla \times \int_{S'} \vec{N} \times \vec{E}(\vec{r}') G_0(\vec{r}, \vec{r}') dS' - \frac{j}{\omega \epsilon} \nabla \times \nabla \times \int_{S'} \vec{N} \times \vec{H}(\vec{r}') G_0(\vec{r}, \vec{r}') dS' \quad (14)$$

where S' is the patch of ocean surface, \vec{N} is the unit normal to the surface S' , \vec{r} is the position vector designating point of observation, \vec{r}' is the position vector designating source field, ϵ is the permittivity of the volume material, and $G_0(r', r)$ is the Green function:

$$G_0(\vec{r}', \vec{r}) = \frac{\exp(-jk|\vec{r} - \vec{r}'|)}{4\pi|\vec{r} - \vec{r}'|} \quad (15)$$

The scattering coefficient of the vertical polarized waves can be defined by the equation in [13]

$$\sigma_v = \frac{4\pi|E_s|^2 R^2}{|E_i|^2 L^2} \quad (16)$$

where E_s is the vertically polarized components of scattered electric field in the position of observation, and R is the distance from scattering patch to the receiver.

2.3. The First-Order Scattering Coefficient

The first-order electric field and magnetic field can be calculated using $A_{mnl}^{(1)}, B_{mnl}^{(1)}, C_{mnl}^{(1)}$. Then the first-order scattering coefficient derived from Formulas (14) and (16) can be expressed as

$$\begin{aligned} \sigma^{(1)}(\omega, \theta_s, \varphi_s) &= 2^4 \pi k_0^4 \times (\sin \theta_s - \cos \varphi_s)^2 \\ &\times \sum_{m=\pm 1} S[k_0(\sin \theta_s \cos \varphi_s - 1), k_0 \sin \theta_s \sin \varphi_s] \delta(\omega - m \omega_B) \end{aligned} \tag{17}$$

where $S(\cdot)$ denotes the ocean directional wavenumber spectrum. The delta-function $\delta(\cdot)$ represents the condition in which Bragg resonance occurs. Thus, ideally, the first-order Bragg peaks located at the the Bragg frequencies of $\pm \omega_B$, are defined by the dispersion equation for deep water

$$\omega_B = \sqrt{g k_B} = \sqrt{g} (k_x^2 + k_y^2)^{1/4} \tag{18}$$

where k_B denotes the magnitude of Bragg wavenumber vector \vec{k}_B , g is the gravitational acceleration, and k_x, k_y are the component of \vec{k}_B in the x and y directions, respectively:

$$\begin{cases} k_x = k_0(\sin \theta_s \cos \varphi_s - 1) \\ k_y = k_0 \sin \theta_s \sin \varphi_s \end{cases} \tag{19}$$

Assuming that the angle of Bragg wave from x axis is β , the $\tan \beta$ can be expressed as

$$\tan \beta = \frac{k_y}{k_x} = \frac{\sin \theta_s \sin \varphi_s}{\sin \theta_s \cos \varphi_s - 1} \tag{20}$$

For the shore-to-air bistatic HF radar, the magnitude of the Bragg wavenumber vector is determined by the radar wavenumber, the scattering angle and the azimuth angle. The direction of the Bragg wavenumber vector is determined by the scattering angle and the azimuth angle.

2.4. The Second-Order Scattering Coefficient

Similar to the derivation of the first-order scattering coefficient, the second-order electromagnetic scattering coefficient can be derived using $A_{mnl}^{(2)}, B_{mnl}^{(2)}, C_{mnl}^{(2)}$

$$\begin{aligned} \sigma^{(2)}_{EM}(\omega, \theta_s, \varphi_s) &= 2^4 \pi k_0^4 (\sin \theta_s - \cos \varphi_s)^2 \\ &\times \sum_{m, m'=\pm 1} \int_{-\infty}^{+\infty} \int_{-\infty}^{+\infty} \left| \frac{A+B}{2} \right|^2 S(m \vec{k}_1) S(m' \vec{k}_2) \delta(\omega - m \sqrt{g k_1} - m' \sqrt{g k_2}) dx dy \end{aligned} \tag{21}$$

where A and B are

$$A = \frac{-\frac{(\vec{k}_0 \cdot \vec{k}_1)(\vec{k}_2 \cdot \vec{k}_s)}{(\sin \theta_s - \cos \varphi_s) \sin \theta_s \cdot k_0^2} - (k_0^2 - (\vec{k}_0 + \vec{k}_1)(\vec{k}_s - \vec{k}_2))}{\sqrt{k_0^2 - (\vec{k}_0 + \vec{k}_1)(\vec{k}_s - \vec{k}_2)}} \tag{22}$$

$$B = \frac{-\frac{(\vec{k}_0 \cdot \vec{k}_2)(\vec{k}_1 \cdot \vec{k}_s)}{(\sin \theta_s - \cos \varphi_s) \sin \theta_s \cdot k_0^2} - (k_0^2 - (\vec{k}_0 + \vec{k}_2)(\vec{k}_s - \vec{k}_1))}{\sqrt{k_0^2 - (\vec{k}_0 + \vec{k}_2)(\vec{k}_s - \vec{k}_1)}} \tag{23}$$

In practice, it is impossible for a vertically polarized wave to propagate exactly parallel to any surface that is imperfect, and satisfy the required boundary conditions at the interface. Both roughness and finite conductivity of the medium below the surface force an effective boundary condition at the mean interface that gives an apparent vertical wave vector component $-k_0 \Delta$. For the rough and

imperfect sea at HF, a typical value of normalized surface impedance Δ is $\Delta \approx 0.011 - i0.012$ [28,29]. The second-order electromagnetic scattering coefficient involving $-k_0\Delta$ can be expressed as

$$\begin{aligned} \sigma^{(2)}_{EM}(\omega, \theta_s, \varphi_s) = & 2^4 \pi k_0^4 (\sin \theta_s - \cos \varphi_s)^2 \\ & \times \sum_{m,m'=\pm 1} \int_{-\infty}^{+\infty} \int_{-\infty}^{+\infty} \left| \frac{A_1 + B_1}{2} \right|^2 S(m\vec{k}_1) S(m'\vec{k}_2) \delta(\omega - m\sqrt{gk_1} - m'\sqrt{gk_2}) dx dy \end{aligned} \tag{24}$$

where A_1 and B_1 are

$$A_1 = \frac{-\frac{(\vec{k}_0 \cdot \vec{k}_1)(\vec{k}_2 \cdot \vec{k}_s)}{(\sin \theta_s - \cos \varphi_s) \sin \theta_s \cdot k_0^2} - (k_0^2 - (\vec{k}_0 + \vec{k}_1)(\vec{k}_s - \vec{k}_2))}{\sqrt{k_0^2 - (\vec{k}_0 + \vec{k}_1)(\vec{k}_s - \vec{k}_2) - k_0\Delta}} \tag{25}$$

$$B_1 = \frac{-\frac{(\vec{k}_0 \cdot \vec{k}_2)(\vec{k}_1 \cdot \vec{k}_s)}{(\sin \theta_s - \cos \varphi_s) \sin \theta_s \cdot k_0^2} - (k_0^2 - (\vec{k}_0 + \vec{k}_2)(\vec{k}_s - \vec{k}_1))}{\sqrt{k_0^2 - (\vec{k}_0 + \vec{k}_2)(\vec{k}_s - \vec{k}_1) - k_0\Delta}}. \tag{26}$$

Electromagnetic coupling coefficient Γ_{EM} can be defined as

$$\Gamma_{EM} = \frac{A_1 + B_1}{2}. \tag{27}$$

The second-order electromagnetic scattering process can be illustrated as in Figure 4. Figure 4 is a view of Figure 2 in the x-y plane. The direction of the radar beam \vec{k}_0 is in the x direction. \vec{k}_s is the projection vector of scattering wave vector \vec{k}_{sc} in the x-y plane. The incident radar wave (wavenumber vector is \vec{k}_0) interacts with the first ocean wave \vec{k}_1 , to produce an intermediate scattered wave \vec{k} . The interactions between an intermediate scattered wave and a second ocean wave \vec{k}_2 , produce a scattered wave \vec{k}_s . These waves obey the constraints

$$\vec{k}_s = \vec{k}_0 + \vec{k}_B \tag{28}$$

and

$$\vec{k}_B = \vec{k}_1 + \vec{k}_2. \tag{29}$$

In addition to the contribution of the second-order electromagnetic scattering, the second-order scattering also contains the contribution of hydrodynamic coupling. The process of hydrodynamic coupling arises from the combination of two ocean waves to produce a second-order ocean wave that generates Bragg scattering. The hydrodynamic coupling coefficient Γ_H in deep water can be found in [30,31]

$$\Gamma_H = \frac{-i}{2} \left[\frac{(\vec{k}_1 \cdot \vec{k}_2 - k_1 k_2)(\omega^2 + \omega_B^2)}{mm' \sqrt{k_1 k_2} (\omega^2 - \omega_B^2)} + k_1 + k_2 \right]. \tag{30}$$

Therefore, the second-order scattering coefficient can be written as

$$\begin{aligned} \sigma^{(2)}(\omega, \theta_s, \varphi_s) = & 2^4 \pi k_0^4 (\sin \theta_s - \cos \varphi_s)^2 \\ & \times \sum_{m,m'=\pm 1} \int_{-\infty}^{+\infty} \int_{-\infty}^{+\infty} |\Gamma|^2 S(m\vec{k}_1) S(m'\vec{k}_2) \delta(\omega - m\sqrt{gk_1} - m'\sqrt{gk_2}) dx dy \end{aligned} \tag{31}$$

where the value of m and m' denotes the four cases of how the two ocean waves are combined. Γ is the sum of the electromagnetic coupling coefficient and the hydrodynamic coupling coefficient

$$\Gamma = \Gamma_H + \Gamma_{EM}. \tag{32}$$

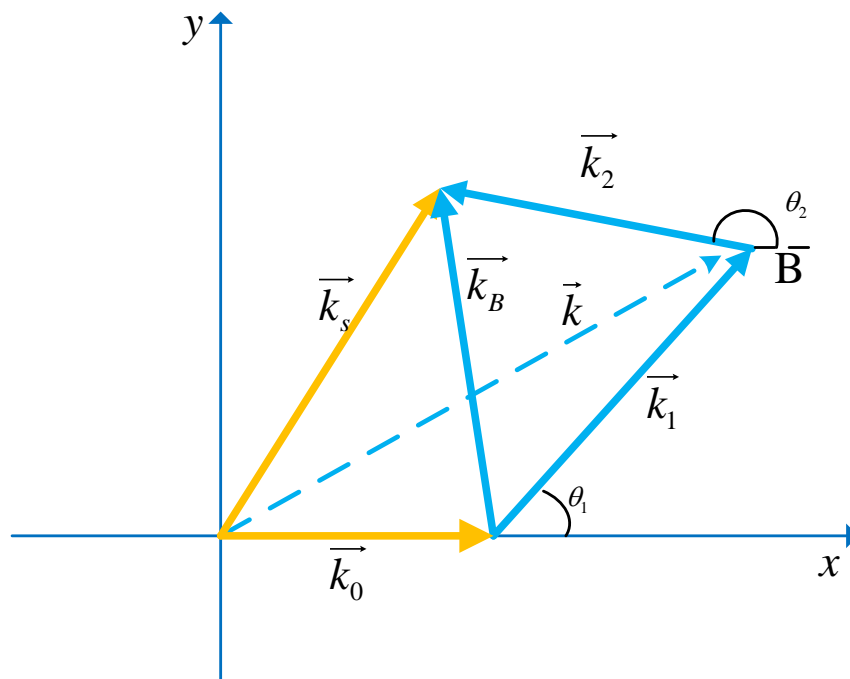


Figure 4. Illustration of the second-order electromagnetic interaction process.

3. Simulation Results and Analysis of the Echo Spectrum

To explore the dependence of the scattering coefficient of a single ocean patch on the environmental parameters, we have employed the Pierson–Moskowitz wave spectrum model [32] with the Longuet–Higgins directional distribution [33] for a wind-driven sea. Many factors, including scattering and azimuthal angles, operating frequencies, and wind speeds and wind directions, are input to the model to examine the effects on the Doppler spectrum.

Figure 5 shows four simulated Doppler spectra for different scattering angles and azimuth angles. The radar operating frequency and wind speed are set to 18 MHz and 12 m/s, respectively. The wind direction is 90° , which is referenced to the direction of the Bragg wave. The first-order Bragg peaks, which have the maxima amplitude, can be seen from the figure at the normalized Bragg frequency $F_B=1$. Figure 5a shows the Doppler spectrum when the scattering angle and azimuth angle are $\theta_s = 90^\circ$, $\varphi_s = 180^\circ$, which is in a monostatic case. Figure 5b shows the Doppler spectrum when the scattering angle and azimuth angle are $\theta_s = 90^\circ$, $\varphi_s = 120^\circ$, respectively, which is in the land-based bistatic case. The singularities at $\pm\sqrt{2}F_B = 1.414$ result from the second-order electromagnetic coupling and the hydrodynamic coupling discussed in [29]. Other singularities at the normalized frequency of $\pm 2^{3/4}F_B$ for monostatic HF radar and at $f_d = \pm 2^{3/4} \sqrt{\frac{(1 \pm \sin \phi_0)^{1/2}}{\cos \phi_0}} F_B$ for land-based bistatic radar, resulting from “corner reflection” condition of second-order electromagnetic scattering [21,29]. Figure 5c,d show the Doppler spectrum in the shore-to-air bistatic radar configuration. Except for the singularities at the normalized frequency of $\pm\sqrt{2}F_B$, there are other singularities resulting from “corner reflection” in the Doppler spectrum. They will be discussed in next section. In addition, the Doppler spectrum is asymmetric about the zero frequency when the wind direction is perpendicular to the direction of reference. This asymmetry is caused by second-order electromagnetic scattering, which is different from monostatic and land-based bistatic cases.

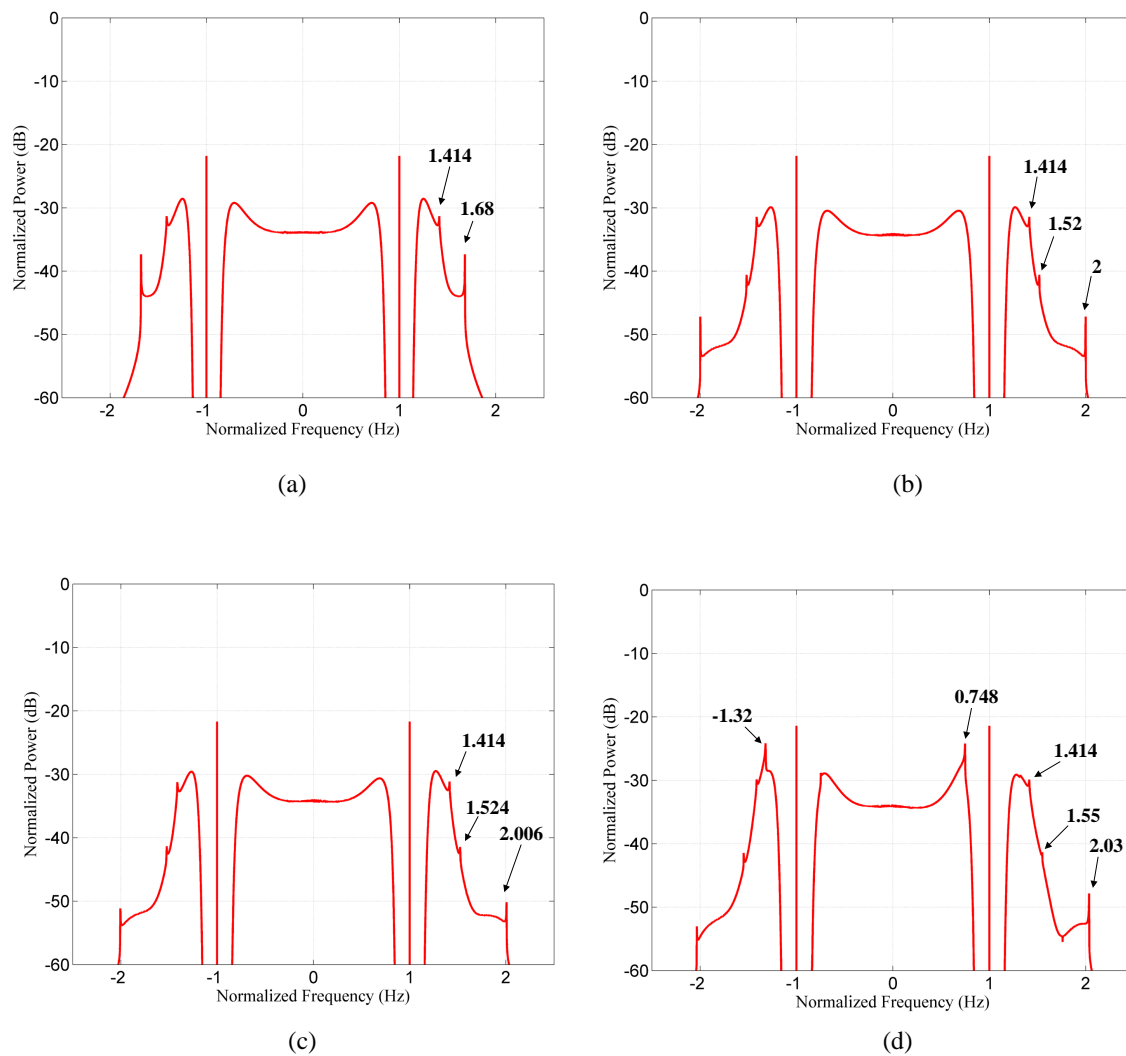


Figure 5. Simulated Doppler spectra for different scattering angles and azimuth angles. The scattering angle and azimuth angle are (a) $\theta_s = 90^\circ$, $\varphi_s = 180^\circ$, (b) $\theta_s = 90^\circ$, $\varphi_s = 120^\circ$, (c) $\theta_s = 75^\circ$, $\varphi_s = 120^\circ$, and (d) $\theta_s = 60^\circ$, $\varphi_s = 120^\circ$.

Figure 6 shows the Doppler spectra at different operating frequencies. The wind speed, wind direction, scattering angle, and azimuth angle are set to 12 m/s, 90° , 60° , and 120° , respectively. It can be noted that the magnitude of the Bragg peaks does not dramatically vary with the change of operating frequency since the Bragg wave is in the saturated zone of the wave height spectrum. The Bragg frequency increases with the operating frequency. The relation between the Bragg frequency and operating frequency can be given by

$$f_B = \left(\frac{g f_0}{2\pi c} \phi \right)^{1/2} \quad (33)$$

where f_0 is the frequency of the electromagnetic wave emitted by radar, c is the speed of light, and $\phi = \sqrt{\sin^2 \theta_s + 1 - 2\sin \theta_s \cos \varphi_s}$. In addition, the magnitude of the Doppler spectra near the first-order peaks increases with the operating frequency as well.

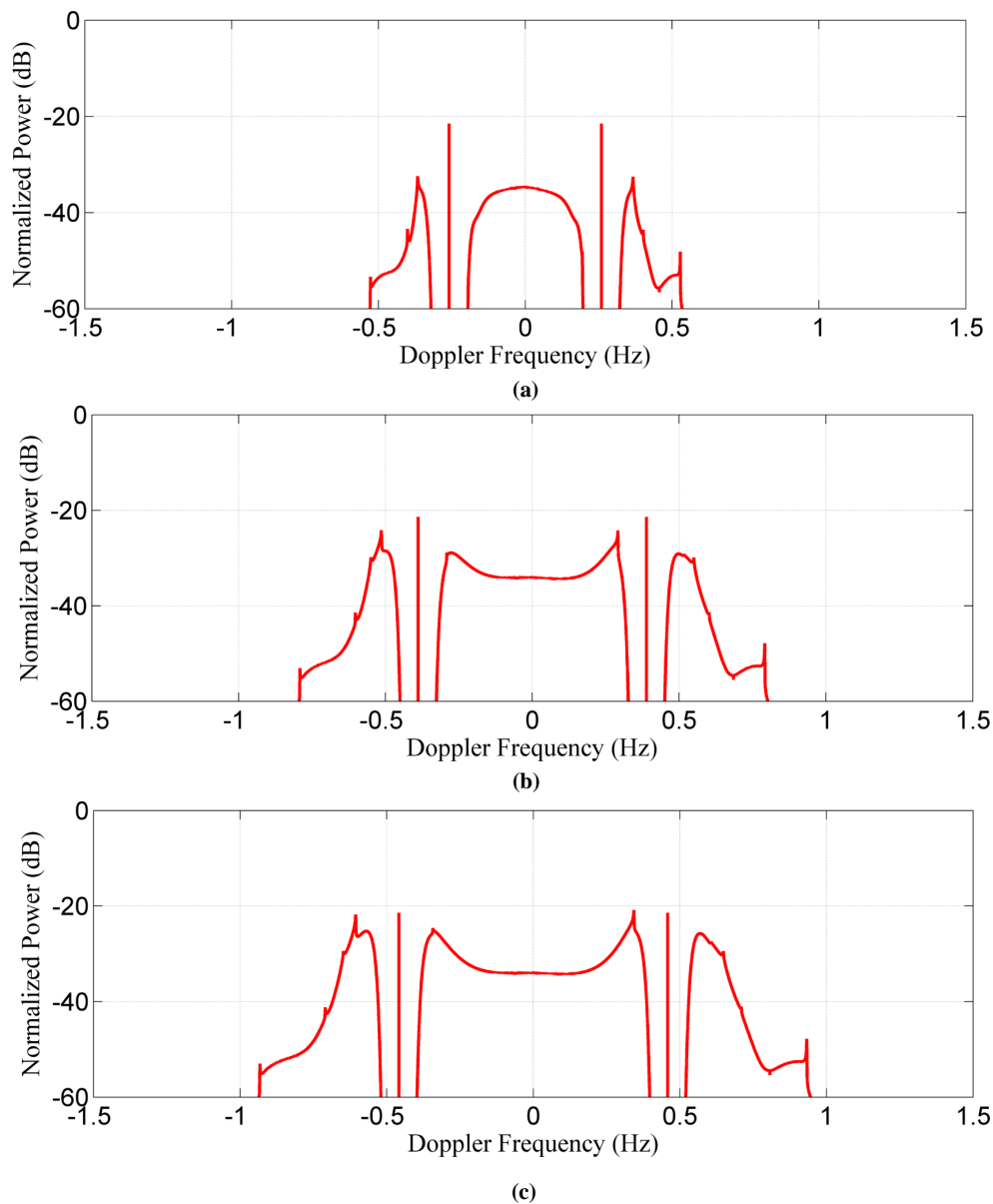


Figure 6. Simulated Doppler spectra at different operating frequencies. The operating frequencies are (a) 8 MHz, (b) 18 MHz, and (c) 25 MHz.

Figure 7 shows the results for different wind speeds. The radar operating frequency, wind direction, scattering angle, and azimuth angle are set to 18 MHz, 90° , 60° , and 120° , respectively. It can be found that the magnitude of the Bragg peaks does not significantly change when the wind speed varies. As aforementioned, this is because the circular frequency of the Bragg wave is about 2.44 rad/s in the above operating status, which indicates that the Bragg wave is fully developed. However, the magnitude of Doppler spectrum near the first-order peaks is sensitive to the wind speed. It indicates that the long ocean waves corresponding to this part of the Doppler spectrum have more energy when wind speed above the ocean surface becomes higher. Just as for monostatic radar, the second-order spectrum can be applied to extract the information of ocean waves [34–37]. Additionally, the magnitude of the second-order spectra far away from Bragg peaks (e.g., at 0.2 Hz and 1.8 Hz) is hardly influenced by the wind speed, since the ocean waves responsible for this portion of the Doppler spectra stay in the saturated region of the ocean spectrum.

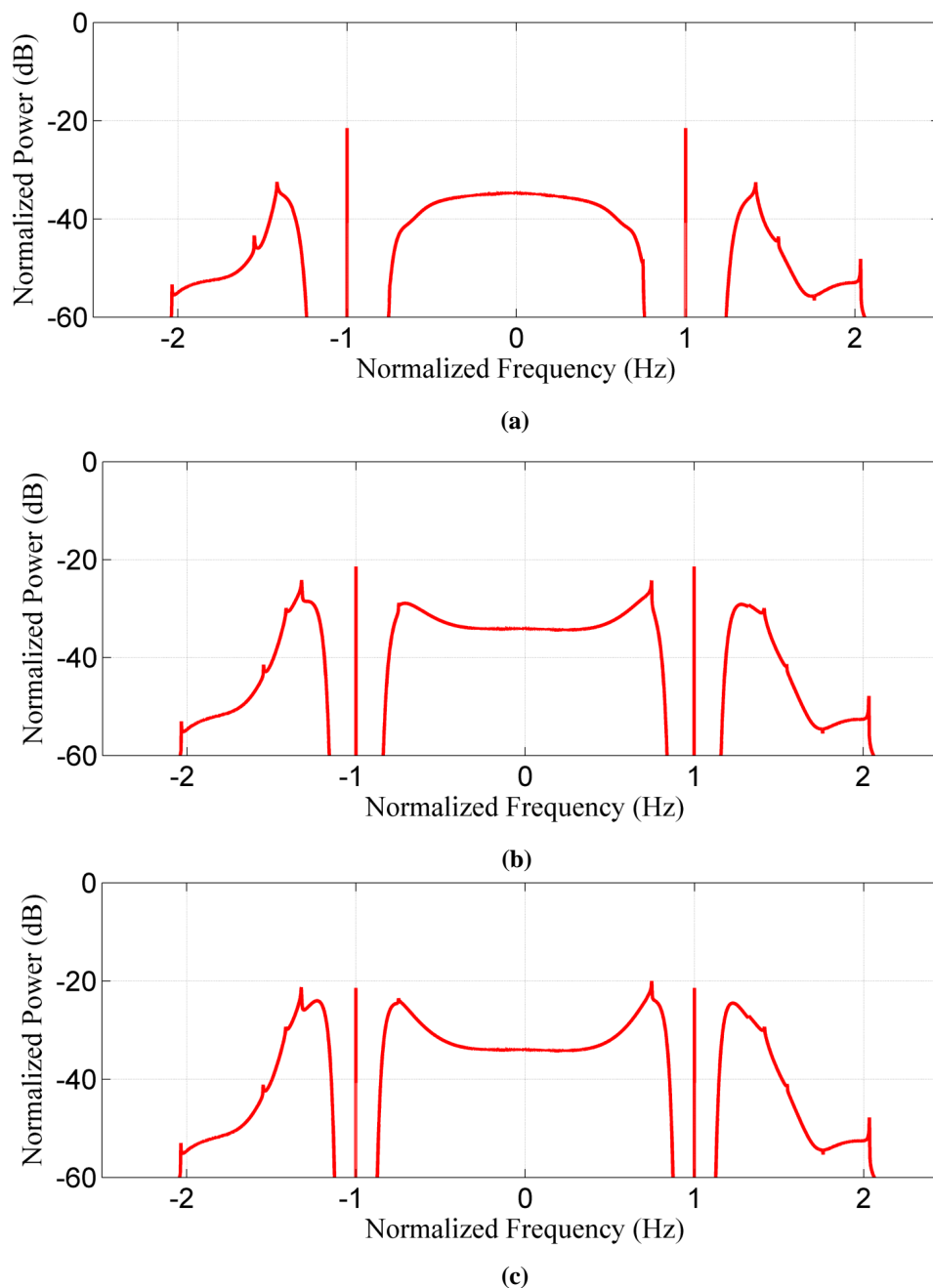


Figure 7. Simulated Doppler spectra with different wind speeds. The wind speed is (a) 8 m/s, (b) 12 m/s, and (c) 15 m/s.

Figure 8 shows the simulated Doppler spectra for different wind directions when the wind speed, scattering angle, and azimuth angle are 12 m/s, 60° , and 120° , respectively. It can be noted that the ratio of the magnitude of the left and right Bragg peaks in the Doppler spectrum varies with the change of wind direction. In the monostatic case, the energy of left and right Bragg peaks is equivalent when the wind direction is perpendicular to the direction of radar beam. In other cases, the energy of one Bragg peak is enhanced and the other will be weakened. For shore-to-air bistatic HF radar, a similar phenomenon occurs, in which the two Bragg peaks do not carry similar amounts of energy when wind direction is not perpendicular to the direction of the Bragg wave. Some researchers have used the ratio of the left and right first-order Bragg peaks to estimate wind direction [38–40].

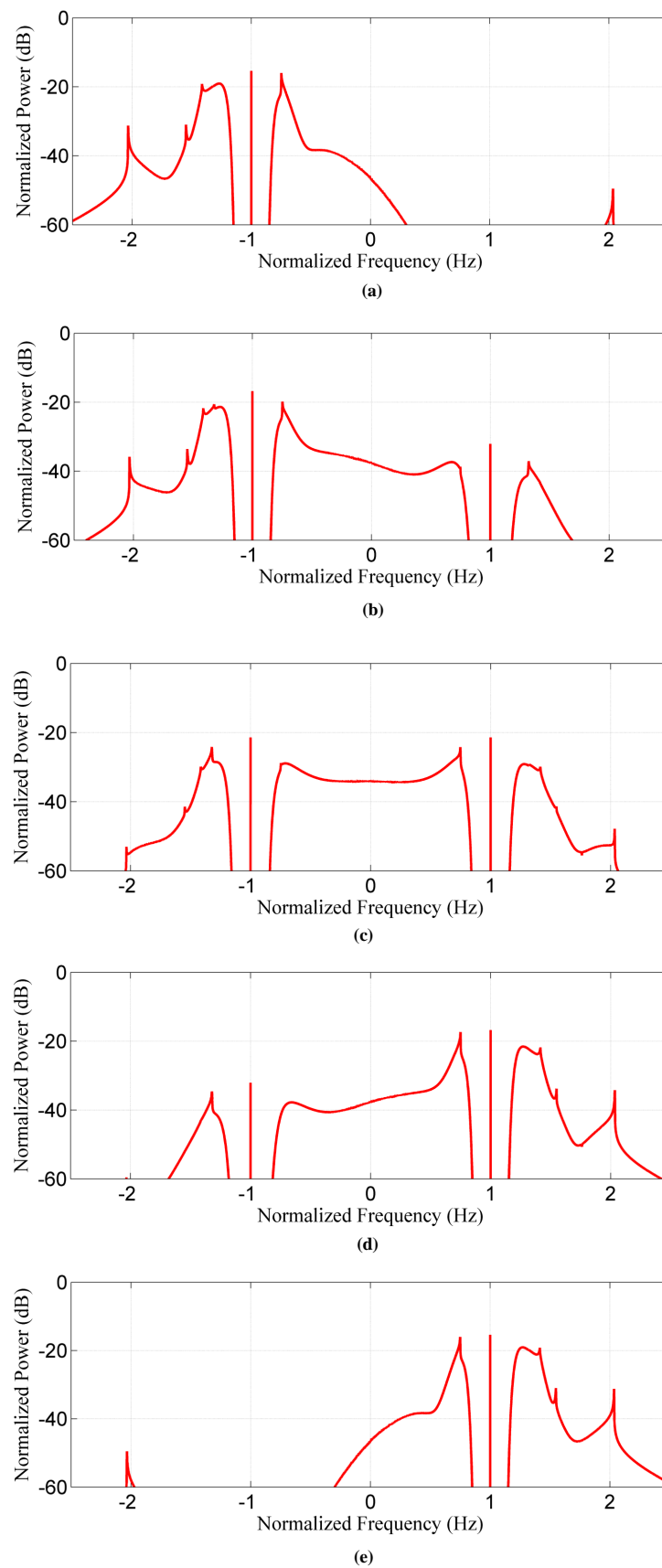


Figure 8. Simulated Doppler spectra with different wind directions. The wind direction is (a) 0° , (b) 45° , (c) 90° , (d) 135° , and (e) 180° .

4. Discussion

The singularities results from “corner reflection” [41], except for the singularity at $\pm\sqrt{2}F_B$ in Figure 5c,d. Taking Figure 5d for example, where the scattering angle and the azimuth angle are $\theta_s = 60^\circ$ and $\varphi_s = 120^\circ$ respectively, additional singularities appear in the simulated Doppler spectrum. The normalized constant Doppler frequency contours are determined by formula (29) and the delta function in (31). Each point on the constant Doppler frequency contour gives a pair of \vec{k}_1 and \vec{k}_2 , as shown in Figure 9. The p axis is parallel to the direction of the Bragg wave, and the contours of constant normalized frequency ω for \vec{k}_1 and \vec{k}_2 satisfy the formulas (29) and (31). The case of “corner reflection” is presented by the black dashed curve, where \vec{k}_1 and \vec{k}_2 satisfy the relation

$$k_0^2 - (\vec{k}_0 + \vec{k}_2)(\vec{k}_s - \vec{k}_1) = 0 \quad (34)$$

or

$$k_0^2 - (\vec{k}_0 + \vec{k}_1)(\vec{k}_s - \vec{k}_2) = 0. \quad (35)$$

The singularities occur where the frequency contour is tangential to the circle of dash curve. Figure 9a shows the normalized constant Doppler frequency contours for $|\omega| > \omega_B$. The frequency contour whose normalized frequency equals 1.32, 1.55, and 2.03 is tangential to the circle of the dash curve. In addition, the singularity at $|\omega| = \sqrt{2}\omega_B$ occurs when the contours separate. Figure 9b shows the normalized constant Doppler frequency contours for $|\omega| < \omega_B$. The normalized frequency equals 0.748 when the frequency contour is tangential to the circle of the dash curve. Therefore, there are ten singularities in the simulated Doppler spectrum at the normalized frequency of $\pm 0.748, \pm 1.32, \pm 1.44, \pm 1.55$, and ± 2.03 , which is the same in Figure 5d.

When the scattering angle and the azimuth angle are $\theta_s = 90^\circ$ and $\varphi_s = 180^\circ$, the first-order and second-order scattering coefficients for shore-to-air bistatic HF radar using the perturbation method will be reduced to the scattering coefficients for monostatic HF radar, which are identical to the result in [29]. The characteristic of the simulated echo spectrum (see Figure 5a) is similar to the characteristic of the simulated spectrum in [29]. Meanwhile, the scattering coefficient for shore-to-air bistatic radar will be reduced to the scattering coefficient of land-based bistatic radar when the scattering angle is $\theta_s = 90^\circ$. While the scattering coefficient for land-based bistatic radar in [21] differs from this work, they have the same forms. The reason is that additional contributions have been incorporated in [21]. The characteristic of the simulated echo spectrum (see Figure 5b) is similar to the characteristic of the simulated spectrum in [21]. It indicates that the scattering coefficient for shore-to-air bistatic radar incorporates the cases of monostatic operation and land-based bistatic operation.

The first-order and second-order scattering coefficients of shore-to-air bistatic HF radar are derived based on the perturbation method. The sea surface needs to satisfy the perturbation condition: $0.2 < \frac{H_s k_0}{2} < 1$, where H_s is the significant wave height, and k_0 is the wavenumber of the radar electromagnetic wave. Therefore, the radar operating frequency determines the limitations of the wave height measurement [42]. For instance, when the operating frequency is 8 MHz, the upper and lower limits of the corresponding significant wave height measurement are about 12 m and 2.4 m, respectively. Whereas at 25 MHz, the upper and lower limits of significant wave height measurement are about 0.7 m and 3.8 m, respectively.

For the bistatic HF radar system where the receiver is deployed on the land or a buoy, the coverage of radar will not be significantly improved comparing with monostatic HF radar since radio waves scattered from the ocean surface to the radar receiver propagate along the sea surface and the attenuation of radio in the receiving path is the same as monostatic HF radar. However, for the shore-to-air bistatic radar, the attenuation of radio in the receiving path is quite small since the radio waves scattered from the ocean surface to the radar receiver propagate in the free space. This advantage will significantly increase the maximum detection range of the radar. In addition, the transmitting and receiving antenna of shore-to-air bistatic radar can be placed in different areas, and this configuration

is flexible, which will reduce the space requirements for radar deployment. Nonetheless, since the receiver is placed on the airborne platform, the size of the receiving antenna will be greatly limited. Therefore, higher requirements are placed on the design of the receiving antenna. A smaller antenna is needed to meet the requirements of size.

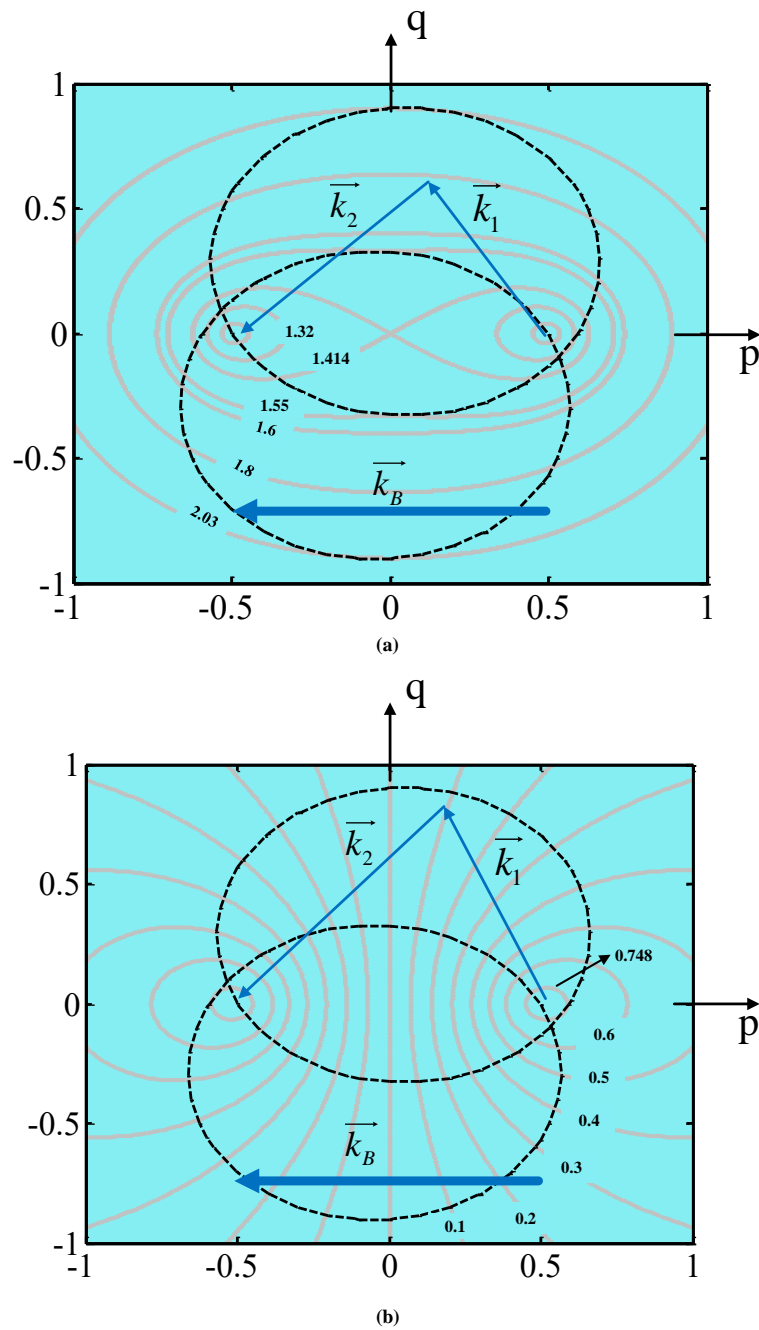


Figure 9. The normalized constant Doppler frequency contours when the scattering angle and the azimuth angle are $\theta_s = 60^\circ$ and $\varphi_s = 120^\circ$, for (a) $|\omega| > \omega_B$ ($m = m'$) and (b) $|\omega| < \omega_B$ ($m \neq m'$). The blue bold arrow denotes the vector of Bragg wave. The normalized constant Doppler frequency contours of ω for \vec{k}_1 and \vec{k}_2 are determined by Formulas (29) and (31) as shown in thin arrows.

5. Conclusions

A new model we have named “shore-to-air bistatic HF radar” has been proposed for ocean observation. The first-order and second-order scattering coefficients for the shore-to-air bistatic radar are derived using the perturbation method. The scattering coefficient of shore-to-air bistatic HF radar can be reduced to the case of monostatic radar when the scattering angle and the azimuth angle are 90° and 180° respectively, which is identical to the result in [29].

The scattering mechanism presented herein between the radar electromagnetic waves and the sea surface may be the foundation for shore-to-air bistatic HF radar development and validation. The Doppler spectra are simulated for various operating conditions and sea states based on the proposed scattering coefficients, which may provide a guideline on the extraction of sea state information using shore-to-air bistatic HF radar. The characteristic of the simulated echo spectrum is similar to the characteristic of the Doppler spectrum for the monostatic and land-based bistatic radar, which verifies the correctness of the developed scattering coefficients. In addition, the singularities in the Doppler spectrum for shore-to-air bistatic radar are analyzed using the normalized constant Doppler frequency contours. Further research will be conducted to apply the proposed scattering coefficients to practical situations.

Author Contributions: Conceptualization, Z.C. and C.Z.; funding acquisition, Z.C. and C.Z.; investigation, J.L., F.D.; Methodology, C.Z., J.L. and F.D.; project administration, Z.C. and C.Z.; software, J.L.; supervision, Z.C. and C.Z.; Validation, J.L., F.D. and X.C.; visualization, J.L.; writing-Original draft, J.L.; writing-review&editing C.Z.

Funding: This research was supported in part by the National Natural Science Foundation of China under Grant 61871296, Grant 41506201, and Grant 41376182, in part by the National Key Research and Development Program of China under Grant 2017YFF0206404 and Grant 2016YFC1400504, in part by the Public Science and Technology Research Funds Projects of Ocean under Grant No. 201205032 in part by Fundamental Research Funds for the Central Universities under Grant 2042018kf1009.

Acknowledgments: The authors would like to thank anonymous reviewers for their valuable comments in improving the quality of this paper.

Conflicts of Interest: The authors declare no conflicts of interest.

Abbreviations

The following abbreviations are used in this manuscript:

HF High frequency
 GIOS Ground-Ionosphere-Ocean-Space

References

- Emery, B.M.; Washburn, L.; Harlan, J.A. Evaluating radial current measurements from CODAR high-frequency radars with moored current meters. *J. Atmos. Ocean. Technol.* **2004**, *21*, 1259–1271. doi:10.1175/1520-0426(2004)021<1259:ERCMFC>2.0.CO;2. [[CrossRef](#)]
- Maresca, S.; Braca, P.; Horstmann, J.; Grasso, R. Maritime surveillance using multiple high-frequency surface-wave radars. *IEEE Trans. Geosci. Remote Sens.* **2013**, *52*, 5056–5071. doi:10.1109/TGRS.2013.2286741. [[CrossRef](#)]
- Shen, W.; Gurgel, K.W. Wind direction inversion from narrow-beam HF radar backscatter signals in low and high wind conditions at different radar frequencies. *Remote Sens.* **2018**, *10*, 1480. doi:10.3390/rs10091480. [[CrossRef](#)]
- Wyatt, L.R.; Green, J.J.; Middleditch, A.; Moorhead, M.D.; Howarth, J.; Holt, M.; Keogh, S. Operational wave, current, and wind measurements with the Pisces HF radar. *IEEE J. Ocean. Eng.* **2006**, *31*, 819–834. doi:10.1109/JOE.2006.888378. [[CrossRef](#)]
- Barrick, D. First-order theory and analysis of MF/HF/VHF scatter from the sea. *IEEE Trans. Antennas Propag.* **1972**, *20*, 2–10. doi:10.1109/TAP.1972.1140123. [[CrossRef](#)]

6. Barrick, D. Remote sensing of sea state by radar. In Proceedings of the Ocean 72-IEEE International Conference on Engineering in the Ocean Environment, Newport, RI, USA, 13–15 September 1972; pp. 186–192. doi:10.1109/OCEANS.1972.1161190. [[CrossRef](#)]
7. Rice, S.O. Reflection of electromagnetic waves from slightly rough surfaces. *Commun. Pure Appl. Math.* **1951**, *4*, 351–378. doi:10.1002/cpa.3160040206. [[CrossRef](#)]
8. Chen, Z.; Zhao, C.; Jiang, Y.; Hu, W. Wave measurements with multi-frequency HF radar in the East China Sea. *J. Electromag. Waves Appl.* **2011**, *25*, 1031–1043. doi:10.1163/156939311795253902. [[CrossRef](#)]
9. Green, J.; Wyatt, L. Row-action inversion of the Barrick–Weber equations. *J. Atmos. Ocean. Technol.* **2006**, *23*, 501–510. doi:10.1175/JTECH1854.1. [[CrossRef](#)]
10. Walsh, J.; Howell, R.; Dawe, B. *Model Development for Evaluation Studies of Ground Wave Radar*; Contract Report; Center Cold Ocean Resources Eng., Mem. Univ. Newfoundland: St. John's, NL, Canada, 1990; pp. 90–C14.
11. Hisaki, Y.; Tokuda, M. VHF and HF sea echo Doppler spectrum for a finite illuminated area. *Radio Sci.* **2001**, *36*, 425–440. doi:10.1029/2000RS002343. [[CrossRef](#)]
12. Hisaki, Y. Doppler spectrum of radio wave scattering from ocean-like moving surfaces for a finite illuminated area. *Int. J. Remote Sens.* **2003**, *24*, 3075–3091. doi:10.1080/01431160210153057. [[CrossRef](#)]
13. Johnstone, D. Second-Order Electromagnetic and Hydromagnetic Effects In High-Frequency Radio-Wave Scattering From the Sea. PhD Thesis, Stanford University, Stanford, CA, USA, 1975.
14. Anderson, S.; Anderson, W. Bistatic HF scattering from the ocean surface and its application to remote sensing of seastate. In Proceedings of the 1987 IEEE APS International Symposium, Blacksburg, VA, USA, 15–19 June 1987.
15. Anderson, S. Limitations to the extraction of information from multi-hop skywave radar signals. In Proceedings of the RADAR, Adelaide, Australia, 3–5 September 2003.
16. Anderson, S.; Fuks, I.; Prashifka, J. Multiple scattering of HF radio waves propagating across the sea surface. *Waves Random Media* **1998**, *8*, 283–302. doi:10.1088/0959-7174/8/3/002. [[CrossRef](#)]
17. Anderson, S. Directional wave spectrum measurement with multistatic HF surface wave radar. In Proceedings of the IGARSS 2000. IEEE 2000 International Geoscience and Remote Sensing Symposium. Taking the Pulse of the Planet: The Role of Remote Sensing in Managing the Environment. Proceedings (Cat. No. 00CH37120), Honolulu, HI, USA, 24–28 July 2000; Volume 7, pp. 2946–2948. doi:10.1109/IGARSS.2000.860299. [[CrossRef](#)]
18. Anderson, S.; Edwards, P.; Marrone, P.; Abramovich, Y. Investigations with SECAR—a bistatic HF surface wave radar. In Proceedings of the International Conference on Radar (IEEE Cat. No. 03EX695), Adelaide, Australia, 3–5 September 2003; pp. 717–722. doi:10.1109/RADAR.2003.1278831. [[CrossRef](#)]
19. Walsh, J.; Gill, E. An analysis of the scattering of high-frequency electromagnetic radiation from rough surfaces with application to pulse radar operating in backscatter mode. *Radio Sci.* **2000**, *35*, 1337–1359. doi:10.1029/2000RS002532. [[CrossRef](#)]
20. Gill, E.; Walsh, J. High-frequency bistatic cross sections of the ocean surface. *Radio Sci.* **2001**, *36*, 1459–1475. doi:10.1029/2000RS002525. [[CrossRef](#)]
21. Gill, E.; Huang, W.; Walsh, J. On the development of a second-order bistatic radar cross section of the ocean surface: a high-frequency result for a finite scattering patch. *IEEE J. Ocean. Eng.* **2006**, *31*, 740–750. doi:10.1109/JOE.2006.886228. [[CrossRef](#)]
22. Huang, W.; Gill, E.; Wu, X.; Li, L. Measurement of sea surface wind direction using bistatic high-frequency radar. *IEEE Trans. Geosci. Remote Sens.* **2012**, *50*, 4117–4122. doi:10.1109/tgrs.2012.2188298. [[CrossRef](#)]
23. Bernhardt, P.A.; Briczinski, S.J.; Siefiring, C.L.; Barrick, D.E.; Bryant, J.; Howarth, A.; James, G.; Enno, G.; Yau, A. Large area sea mapping with Ground-Ionosphere-Ocean-Space (GIOS). In Proceedings of the OCEANS 2016 MTS/IEEE Monterey, Monterey, CA, USA, 19–23 September 2016; pp. 1–10. doi:10.1109/OCEANS.2016.7761503. [[CrossRef](#)]
24. Bernhardt, P.A.; Siefiring, C.L.; Briczinski, S.C.; Vierinen, J.; Miller, E.; Howarth, A.; James, H.G.; Blincoe, E. Bistatic observations of the ocean surface with HF radar, satellite and airborne receivers. In Proceedings of the IEEE OCEANS 2017-Anchorage, Anchorage, AK, USA, 18–21 September 2017; pp. 1–5.
25. Voronovich, A.G.; Zavorotny, V.U. Measurement of ocean wave directional spectra using airborne HF/VHF synthetic aperture radar: A theoretical evaluation. *IEEE Trans. Geosci. Remote Sens.* **2017**, *55*, 3169–3176. doi:10.1109/TGRS.2017.2663378. [[CrossRef](#)]

26. Zhao, C.; Chen, Z. Model of shore-to-air bistatic HF radar for ocean observation. In Proceedings of the OCEANS 2018 MTS/IEEE Charleston, Charleston, SC, USA, 22–25 October 2018; pp. 1–4. doi:10.1109/OCEANS.2018.8604581. [CrossRef]
27. Tai, C.T. Kirchhoff theory: scalar, vector, or dyadic? *IEEE Trans. Antennas Propag.* **1972**, *20*, 114–115. doi:10.1109/TAP.1972.1140146. [CrossRef]
28. Barrick, D.E. Theory of HF and VHF propagation across the rough sea, 1, The effective surface impedance for a slightly rough highly conducting medium at grazing incidence. *Radio Sci.* **1971**, *6*, 517–526. doi:10.1029/RS006i005p00517. [CrossRef]
29. Lipa, B.J.; Barrick, D.E. Extraction of sea state from HF radar sea echo: Mathematical theory and modeling. *Radio Sci.* **1986**, *21*, 81–100. doi:10.1029/RS021i001p00081. [CrossRef]
30. Barrick, D.; Weber, B. On the nonlinear theory for gravity waves on the ocean's surface. Part II: Interpretation and applications. *J. Phys. Oceanogr.* **1977**, *7*, 11–21. doi:10.1175/1520-0485(1977)007<0011:OTNTFG>2.0.CO;2. [CrossRef]
31. Weber, B.; Barrick, D. On the nonlinear theory for gravity waves on the ocean's surface. Part I: Derivations. *J. Phys. Oceanogr.* **1977**, *7*, 3–10. doi:10.1175/1520-0485(1977)007<0003:OTNTFG>2.0.CO;2. [CrossRef]
32. Moskowitz, L. Estimates of the power spectrums for fully developed seas for wind speeds of 20 to 40 knots. *J. Geophys. Res.* **1964**, *69*, 5161–5179. doi:10.1029/JZ069i024p05161. [CrossRef]
33. Longuet-Higgins, M.S. Observations of the directional spectrum of sea waves using the motions of a floating buoy. *Ocean Wave Spectra* **1961**. doi:10.1007/BF02861508. [CrossRef]
34. Howell, R.; Walsh, J. Measurement of ocean wave spectra using narrow-beam HE radar. *IEEE J. Ocean. Eng.* **1993**, *18*, 296–305. doi:10.1109/JOE.1993.236368. [CrossRef]
35. Gill, E.; Khandekar, M.; Howell, R.; Walsh, J. Ocean surface wave measurement using a steerable high-frequency narrow-beam ground wave radar. *J. Atmos. Ocean. Technol.* **1996**, *13*, 703–713. doi:10.1175/1520-0426(1996)013<0703:OSWMUA>2.0.CO;2. [CrossRef]
36. Huang, W.; Wu, S.; Gill, E.; Wen, B.; Hou, J. HF radar wave and wind measurement over the Eastern China Sea. *IEEE Trans. Geosci. Remote Sens.* **2002**, *40*, 1950–1955. doi:10.1109/TGRS.2002.803718. [CrossRef]
37. Barrick, D.E. Extraction of wave parameters from measured HF radar sea-echo Doppler spectra. *Radio Sci.* **1977**, *12*, 415–424. doi:10.1029/RS012i003p00415. [CrossRef]
38. Heron, M.L.; Prytz, A. Wave height and wind direction from the HF coastal ocean surface radar. *Can. J. Remote Sens.* **2002**, *28*, 385–393. doi:10.5589/m02-031. [CrossRef]
39. Wyatt, L.R. An evaluation of wave parameters measured using a single HF radar system. *Can. J. Remote Sens.* **2002**, *28*, 205–218. doi:10.5589/m02-018. [CrossRef]
40. Zeng, Y.; Zhou, H.; Lai, Y.; Wen, B. Wind-Direction Mapping With a Modified Wind Spreading Function by Broad-Beam High-Frequency Radar. *IEEE Geosci. Remote Sens. Lett.* **2018**, *15*, 679–683. doi:10.1109/LGRS.2018.2809558. [CrossRef]
41. Ivonin, D.V.; Shrira, V.I.; Broche, P. On the singular nature of the second-order peaks in HF radar sea echo. *IEEE J. Ocean. Eng.* **2006**, *31*, 751–767. doi:10.1109/joe.2006.886080. [CrossRef]
42. Wyatt, L.R.; Green, J.J.; Middleditch, A. HF radar data quality requirements for wave measurement. *Coastal Eng.* **2011**, *58*, 327–336. doi:10.1016/j.coastaleng.2010.11.005. [CrossRef]

